

JOURNAL GEUTHEE OF ENGINEERING AND ENERGY

Homepage : https://joge.geutheeinstitute.com/index.php/jogee

Unsupervised operating-regime and anomaly-candidate discovery in field photovoltaic measurements under incremental conductance MPPT

Giovanni Dimas Prenata[1*], Ahmad Ridho'i[2]
[1,2]Department of Electrical Engineering, Universitas 17 Agustus 1945 Surabaya, Indonesia
**Corresponding Author: gprenata@untag-sby.ac.id*

ABSTRACT

Field photovoltaic measurements exhibit nonlinear environmental variation, heterogeneous module responses, and scarce verified fault labels, making fixed-threshold anomaly screening difficult. This study develops an unsupervised framework for operating-regime and anomaly-candidate discovery from a limited field dataset consisting of only 81 observations collected from three photovoltaic modules over five measurement days under Incremental Conductance MPPT. Ten environmental, temporal, electrical, and physics-related features were robustly normalized using the median and interquartile range and evaluated with K-Means, Fuzzy C-Means, Gaussian Mixture Model, DBSCAN, and K-Medoids. Model selection combined internal validity, minimum cluster-size constraints, repeated-run stability, ordinal-rank consensus, and composite anomaly scoring. Among the tested configurations, DBSCAN achieved the highest internal validity, with a Silhouette coefficient of 0.3751 and a Davies–Bouldin index of 0.8749, while K-Medoids showed high repeated-run stability (mean ARI=0.9655) and strong agreement with DBSCAN on non-noise observations (ARI=0.9301). The consensus identified Low, Moderate, and High operating regimes containing 16, 26, and 39 observations, respectively. The mutually exclusive anomaly categorization identified five high-score anomaly candidates, seven density-supported candidates, and 69 non-anomalous observations. Because verified fault labels and independent full I–V sweep references were unavailable, the selected observations are interpreted as candidates for targeted physical inspection rather than confirmed photovoltaic faults. The framework therefore provides a structured basis for exploratory screening of field photovoltaic measurements.

Keywords: Anomaly Candidate; DBSCAN; Incremental Conductance MPPT; Operating-Regime Discovery; Unsupervised Learning

Manuscript received 15 Oct. 2021; revised 29 Jan. 2022; accepted 2 May. 2022. Date of publication 17 May. 2022.
Journal Geuthee of Engineering and Energy is licensed under a Creative Commons Attribution-Share Alike 4.0 International License.

1. INTRODUCTION

Photovoltaic power conversion is governed by nonlinear electrical characteristics that change continuously with irradiance, module temperature, loading conditions, and module technology. Consequently, a photovoltaic system does not operate at a fixed voltage or current. Maximum power point tracking is therefore required to move the operating point toward the region where the product of voltage and current is maximized. Incremental Conductance MPPT determines the tracking direction from the relationship between incremental and instantaneous conductance, and its performance is strongly associated with environmental changes and

measurement dynamics [1] [2]. Although Incremental Conductance MPPT seeks effective power extraction, field voltage, current, and power still vary with irradiance transients, temperature, sensor limitations, converter response, shading, and module mismatch. Consequently, a fixed threshold can confuse normal environmental variation with behavior that deserves inspection.

Previous PV monitoring studies have used model- or threshold-based indicators [3], one-class residual monitoring without multiclass fault labels [4], density-based data-stream clustering [5], and unsupervised classification with local outlier detection [6]. Collectively, these studies motivate label-free operating-regime separation before anomaly assessment. No single clustering algorithm fully describes the data structure. K-Means represents centroid-based groups [7], Fuzzy C-Means (FCM) models gradual memberships [8], Gaussian Mixture Models (GMM) provide probabilistic components [9], DBSCAN identifies dense regions and noise [10], and K-Medoids uses measured observations as cluster representatives [11].

Because these methods impose different geometric, fuzzy, probabilistic, and density assumptions, their agreement and disagreement provide complementary evidence. A consensus can summarize the shared low-to-high operating structure, whereas inconsistent assignments can contribute to anomaly scoring. Without ground-truth operating-regime labels, clustering quality was evaluated using the Silhouette coefficient [12], Davies–Bouldin index [13], Caliński–Harabasz index [14], and adjusted Rand index (ARI) for partition agreement and repeated-run stability [15]. An unusual PV observation may arise from low probabilistic density, weak fuzzy membership, large centroid or medoid distance, sparse local neighbors, power mismatch, or cross-method disagreement. Combining these indicators avoids reducing anomaly detection to a single distance or residual threshold.

Related work by Prenata and co-authors provides methodological context for the present study. Unsupervised K-Means and Fuzzy C-Means clustering has been used to reveal structured dielectric-degradation patterns in contaminated transformer-oil measurements [16] and transitional thermal-behavior patterns in high-voltage electrical equipment [17]. In electrical condition monitoring, Fourier-domain analysis of motor current has also been used to distinguish bearing-fault patterns [18], while a limited-data ECG study emphasized comparative model evaluation, repeated runs, and cautious interpretation under small-sample conditions [19]. Within JOGE, photovoltaic monitoring through IoT [20], evaluation of solar-powered public street lighting [21], and electrical-condition detection based on measured current signals [18] further demonstrate the relevance of data-driven monitoring in energy and electrical systems. However, these studies do not address consensus-based operating-regime discovery and anomaly-candidate screening from limited field photovoltaic measurements under Incremental Conductance MPPT. The present study addresses this gap through complementary unsupervised models, ordinal consensus, and mutually exclusive anomaly-candidate categories.

This study investigates unsupervised operating-regime and anomaly-candidate discovery from limited field measurements of three PV modules under Incremental Conductance MPPT. Module identity and datasheet values are excluded from clustering so that the unknown-specification P3 module is not separated by metadata. The analysis asks whether stable operating regimes can be discovered and which observations remain unusual across complementary unsupervised criteria. The contributions are: (1) a common ten-feature comparison of K-Means, FCM, GMM, DBSCAN, and K-Medoids; (2) model selection constrained by internal validity and minimum cluster size; (3) ordinal-rank consensus across different cluster counts; and (4) a composite anomaly score separating high-score from density-supported candidates. Because verified fault labels are unavailable, all detections are reported as anomaly candidates rather than confirmed faults.

2. RESEARCH METHOD

2.1. Dataset, Derived Quantities, and Feature Construction

The dataset consisted of 81 observations obtained from modules P1, P3, and P5 over five measurement days. Each row contained the day, measurement time, module identity, technology metadata, open-circuit voltage (V_{oc}), short-circuit current (I_{sc}), battery voltage (V_{bat}), battery current (I_{bat}), irradiance (G), temperature (T), estimated maximum-power-point voltage ($V_{mp,est}$),

and estimated maximum-power-point current ($I_{mp,est}$). The executed program confirmed the use of 81 observations, five days, ten clustering features, and robust median–IQR normalization. Battery-side power was calculated as

$$P_{\mathrm{bat},i} = V_{\mathrm{bat},i} I_{\mathrm{bat},i} \tag{1}$$

The available estimated maximum-power-point power was calculated as

$$P_{\mathrm{MPP,est},i} = V_{\mathrm{mp,est},i} I_{\mathrm{mp,est},i} \tag{2}$$

The power residual was defined by

$$\Delta P_i = P_{\mathrm{bat},i} - P_{\mathrm{MPP,est},i} \tag{3}$$

and the relative residual was

$$r_{\Delta P,i} = \frac{\Delta P_i}{\max(|P_{\mathrm{MPP,est},i}|,1)} \tag{4}$$

The denominator lower bound prevents unstable division near zero. Because PMPP,est is derived from available Incremental-Conductance quantities rather than an independent full I–V sweep, ΔP is treated as an empirical battery-to-estimated-MPP mismatch rather than direct MPPT efficiency.

Table 1. Ten-dimensional operating feature set

No.	Feature	Mathematical representation	Purpose
1	Irradiance	G	Available solar input
2	Temperature	T	Thermal operating condition
3	Decimal time	t	Daily temporal position
4	Open-circuit voltage	Voc	Module voltage characteristic
5	Short-circuit current	Isc	Irradiance-sensitive current characteristic
6	Battery-voltage ratio	Vbat/Voc	Relative voltage operating point
7	Battery-current ratio	Ibat/Isc	Relative current operating point
8	Estimated power per irradiance	PMPP,est/G	Normalized estimated-power response
9	Battery power per irradiance	Pbat/G	Normalized measured-power response
10	Relative residual	rΔP	Mismatch between battery and estimated MPP power

Module identity, technology labels, specification flags, and datasheet coefficients were excluded from clustering to avoid metadata-driven separation and artificial zero-valued specifications for P3. Features were then robustly scaled using the median and interquartile range:

$$z_{ij} = \mathrm{clip}\left(\frac{x_{ij} - \tilde{x}_j}{\mathrm{IQR}_j}, -6,6\right) \tag{5}$$

where x̃j and IQRj are the median and interquartile range of feature j. Zero-IQR features used one-quarter of the observed range and then one as a fallback; standardized values were clipped to limit the influence of extremes.

2.2. Clustering, Model Selection, and Consensus Construction

Candidate K values from 2 to 6 were tested for K-Means, FCM, GMM, and K-Medoids. Each candidate used 30 deterministic runs; maximum iterations were 200, 250, 300, and 120, respectively. Stability was evaluated through 20 additional reruns, and every feasible cluster required at least three observations.

A. K-Means

K-Means minimizes the within-cluster squared-distance objective [7]:

$$J_{\mathrm{KM}} = \sum_{i=1}^{N} \left\| \mathbf{z}_i - \boldsymbol{\mu}_{c_i} \right\|_2^2 \tag{6}$$

where μci is the centroid assigned to observation i. K-Means and K-Medoids candidate partitions were ranked using the following program-specific composite internal score:

$$S_{\mathrm{part}} = S_{\mathrm{sil}} + \frac{0.15}{1+\mathrm{DBI}} + 0.015\ln(1+\mathrm{CH}) - 0.015(K-2) \tag{7}$$

where Ssil, DBI, and CH are the Silhouette, Davies–Bouldin, and Caliński–Harabasz indices; the final term penalizes unnecessary cluster proliferation.

B. Fuzzy C-Means

FCM represents each observation using memberships uic ∈ [0,1] and minimizes [8]:

$$J_{\mathrm{FCM}} = \sum_{i=1}^{N}\sum_{c=1}^{K} u_{ic}^{m} \left\|\mathbf{z}_i - \mathbf{v}_c\right\|_2^2 \tag{8}$$

subject to

$$\sum_{c=1}^{K} u_{ic} = 1 \tag{9}$$

with fuzzifier m=2. The FCM selection score augmented the common internal score with the partition coefficient (PC) and partition entropy (PE):

$$S_{\mathrm{FCM}} = S_{\mathrm{part}} + 0.05\,PC - 0.05\,PE \tag{10}$$

Higher PC and lower PE favor crisper memberships while retaining geometric separation.

C. Gaussian Mixture Model

The GMM assumed a mixture of K diagonal Gaussian components [9]:

$$p(\mathrm{z}_i) = \sum_{c=1}^{K} \pi_c\, \mathcal{N}(\mathrm{z}_i \mid \mu_c, \Sigma_c) \tag{11}$$

where πc, μc, and Σc are the component weight, mean, and diagonal covariance. Parameters were estimated by expectation–maximization, and the lowest BIC among feasible solutions was selected.

$$\mathrm{BIC} = -2\ln\hat{L} + p\ln N \tag{12}$$

where L̂ is the maximized likelihood and p is the number of estimated parameters.

D. DBSCAN

DBSCAN defines an ε-neighborhood [10]:

$$\mathcal{N}_{\varepsilon}(\mathbf{z}_i) = \left\{\mathbf{z}_j : \left\|\mathbf{z}_j - \mathbf{z}_i\right\|_2 \le \varepsilon\right\} \tag{13}$$

A point is core when its ε-neighborhood contains at least minPts observations; non-density-reachable points are noise. The search used minPts=3–7 and 17 ε candidates from nearest-neighbor-distance quantiles 0.15–0.95. Feasible solutions required 2–6 clusters, at least three members per cluster, and ≤40% noise.

$$S_{\mathrm{DBSCAN}} = S_{\mathrm{sil}}(1 - \rho_{\mathrm{noise}}) + \frac{0.15}{1+\mathrm{DBI}} + 0.010\ln(1 + \mathrm{CH}) - 0.20\rho_{\mathrm{noise}} \tag{14}$$

where ρnoise is the noise fraction.

E. K-Medoids

K-Medoids minimizes the total dissimilarity to representative observations [11]:

$$J_{\mathrm{KMd}} = \sum_{i=1}^{N} \min_{m\in\mathcal{M}} d(\mathbf{z}_i, \mathbf{z}_m) \tag{15}$$

where M is the set of medoid indices; unlike a centroid, each medoid is an actual measured observation.

F. Internal Validation and Stability

For each observation, the Silhouette value was calculated as [12]:

$$s(i) = \frac{b(i) - a(i)}{\max\{a(i), b(i)\}} \tag{16}$$

where a(i) is the mean within-cluster distance and b(i) is the lowest mean distance to another cluster. The Davies–Bouldin index was calculated as [13]:

$$\mathrm{DBI} = \frac{1}{K}\sum_{c=1}^{K} \max_{l\neq c} \frac{\sigma_c + \sigma_l}{d(\boldsymbol{\mu}_c, \boldsymbol{\mu}_l)} \tag{17}$$

where lower values indicate better separation. The Caliński–Harabasz index was expressed as [14]:

$$\mathrm{CH} = \frac{B_K/(K-1)}{W_K/(N-K)} \tag{18}$$

where BK and WK are between- and within-cluster dispersions; higher values are preferred. Repeated-run stability and pairwise agreement were evaluated using ARI [15].

G. Ordinal-Rank Consensus

The consensus cluster count was the median of the five selected cluster counts. Within each method, clusters were ordered by mean battery-side power and converted to normalized ordinal ranks $r_{im} \in [0,1]$. The consensus rank was

$$\overline{r}_i = \frac{1}{M_i}\sum_{m=1}^{M_i} r_{im} \tag{19}$$

where DBSCAN was omitted for observations marked as noise. The consensus label was then obtained from

$$c_i^{\mathrm{con}} = \mathrm{round}[\overline{r}_i(K_{\mathrm{con}} - 1)] \tag{20}$$

Cross-method disagreement was the standard deviation of available ordinal ranks and was retained as an anomaly-score component.

2.3. Composite Anomaly Scoring

Seven anomaly components were used: GMM negative log-density, K-Means centroid distance, FCM uncertainty, K-Medoids medoid distance, local density with DBSCAN-noise support, cross-method ordinal disagreement, and absolute relative power residual. Each component was converted to an empirical percentile rank $q_{ih} \in [0,1]$. The composite score was

$$A_i = 0.22q_{i,\mathrm{GMM}} + 0.10q_{i,\mathrm{KM}} + 0.10q_{i,\mathrm{FCM}} + 0.13q_{i,\mathrm{KMd}} + 0.20q_{i,\mathrm{density}} + 0.15q_{i,\mathrm{disagreement}} + 0.10q_{i,\mathrm{residual}} \quad (21)$$

The weights sum to one, with the largest contributions assigned to GMM density and DBSCAN-related local density. The initial robust threshold was

$$A_{\mathrm{IQR}} = Q_3(A) + 1.5\,\mathrm{IQR}(A) \quad (22)$$

Because the score lies in [0,1], the 95th percentile replaced an IQR upper fence above one, with a minimum safeguard of 0.70:

$$A_{\mathrm{main}} = \max\left[0.70, \begin{cases} A_{\mathrm{IQR}}, & A_{\mathrm{IQR}} \le 1, \\ Q_{0.95}(A), & A_{\mathrm{IQR}} > 1. \end{cases}\right] \quad (23)$$

To make the selection criteria mutually exclusive, an observation was assigned to the high-score anomaly-candidate group when

$$A_i \ge A_{\mathrm{main}} \quad (24)$$

An observation was assigned to the density-supported candidate group only when

$$(\mathrm{DBSCAN\ noise_i} = 1) \wedge (\mathrm{Q_3(A)} \le \mathrm{A_i} < \mathrm{A_{main}}) \quad (25)$$

All remaining observations were classified as non-anomalous. Thus, the final result categories were mutually exclusive: high-score anomaly candidates, density-supported candidates, and non-anomalous observations. A separate physical diagnostic flag tested the following questionable relationships:

$$I_{\mathrm{bat}} > I_{\mathrm{sc}}, \qquad V_{\mathrm{bat}} \ge V_{\mathrm{oc}} \quad (26)$$

$$P_{\mathrm{MPP,est}} > 1.05 V_{\mathrm{oc}} I_{\mathrm{sc}} \quad (27)$$

or when either power quantity was negative. This diagnostic flag was used only for post-analysis comparison, not as a clustering or ground-truth fault label. Figure 1 summarizes the workflow.

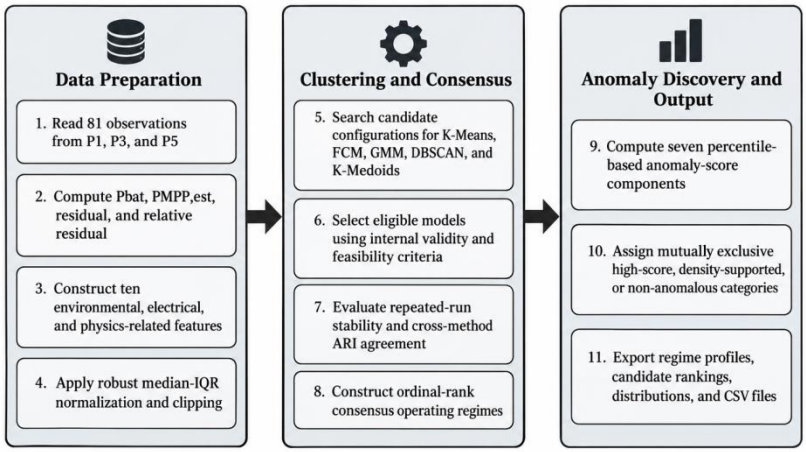


Figure 1. Sequential workflow implemented in model.

3. RESULTS AND DISCUSSION

3.1. Clustering-Model Selection, Internal Validity, and Stability

The selected solutions differed substantially in their preferred number of operating regimes. K-Means and FCM selected two clusters, GMM selected three, and DBSCAN and K-Medoids selected five. The consensus procedure subsequently produced three operating regimes. This variation is expected because centroid, fuzzy, probabilistic, density-based, and medoid algorithms represent different aspects of the same ten-dimensional data structure.

Table 2. Selected clustering configurations and internal validation

Method	Selected (K)	Noise	Silhouette	DBI	CH	SSE	Stability ARI, mean ± SD
K-Means	2	0	0.2657	1.7090	19.2927	379.303	0.1261 ± 0.1158
Fuzzy C-Means	2	0	0.2459	1.7310	20.8128	373.526	1.0000 ± 0.0000
GMM	3	0	0.2623	1.3828	21.4530	304.458	0.6073 ± 0.4136
DBSCAN	5	14	0.3751	0.8749	28.0413	95.079	–
K-Medoids	5	0	0.3116	1.1095	27.9712	190.898	0.9655 ± 0.0483
Consensus	3	0	0.2206	1.9355	14.9521	341.143	–

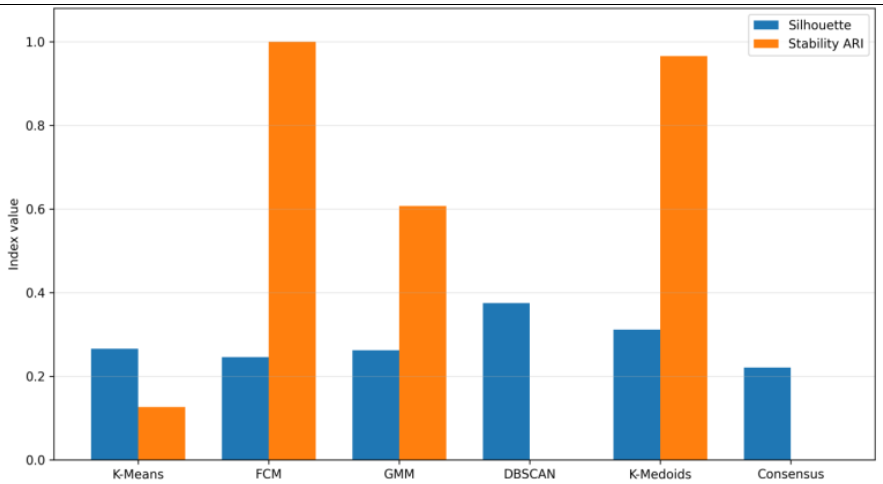


Figure 2. Internal cluster separation and repeated-run stability of the selected models.

Among the tested configurations, DBSCAN achieved the highest internal validity (Silhouette 0.3751, DBI 0.8749, CH 28.0413), with 14 observations treated as noise and 67 forming five density-connected groups. Its selected parameters were ε=1.395695 and minPts=3. This internal-validity result should be interpreted together with the 17.28% noise rate; the selection score therefore penalized excessive noise rather than rewarding separation alone.

K-Medoids offered the strongest balance between separation and reproducibility: Silhouette=0.3116 and stability ARI=0.9655±0.0483. Its five-state solution also uses measured observations as medoids, improving physical traceability. FCM was perfectly stable across reruns (ARI=1.0000) but had weaker separation (Silhouette=0.2459, DBI=1.7310), indicating a reproducible broad low/high split rather than detailed local structure.

GMM selected three components (BIC=1468.8176) with moderate but variable stability (0.6073±0.4136), consistent with initialization sensitivity in a limited ten-dimensional dataset. K-Means was least stable (ARI=0.1261). Although K=3 reached Silhouette=0.5064, it was rejected because a cluster contained fewer than three observations; the feasible K=2 solution was retained.

Likewise, lower-BIC GMM solutions with four to six components were rejected because they produced undersized components, preventing structurally degenerate model selection. The consensus Silhouette of 0.2206 was expectedly lower because consensus was designed to reconcile ordinal low-to-high ranks across methods, not to maximize Euclidean separation.

3.2. Physical Interpretation of the Consensus Operating Regimes

The consensus solution contained 16 Low-regime observations, 26 Moderate-regime observations, and 39 High-regime observations. The regime order was established from mean battery-side power rather than from predefined class labels. This power-based ordering provides a physically interpretable reference for comparing the multivariate characteristics of each regime without imposing external class labels. The regime profiles were therefore summarized using irradiance, temperature, Voc, Isc, battery-side power, estimated MPP power, residual behavior, and anomaly scores. These variables allow the consensus structure to be interpreted in terms of both environmental input and electrical response, as summarized in Table 3.

Table 3. Consensus operating-regime profiles

Variable	Low	Moderate	High
Number of observations	16	26	39
Dataset proportion (%)	19.75	32.10	48.15
Mean irradiance (W/m^2)	142.29	480.10	873.34
Mean temperature (°C)	34.03	41.50	50.00
Mean V_{oc} (V)	18.72	19.38	19.81
Mean I_{sc} (A)	0.458	1.983	4.549
Mean relative residual	−0.2201	−0.0436	−0.3216
Mean P_{bat} (W)	4.77	27.15	45.89
Mean $P_{MPP,est}$ (W)	6.36	28.36	67.22
Mean residual (W)	−1.59	−1.20	−21.33
Mean anomaly score	0.5691	0.6563	0.3696
Anomaly candidates	2	7	3

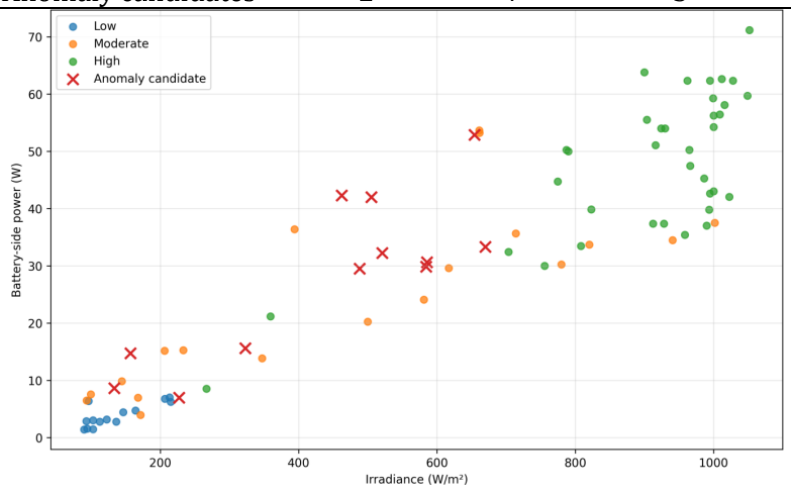


Figure 3. Consensus operating regimes in the irradiance–battery-power plane; crosses denote anomaly candidates.

The Low regime reflected weak input (142.29 W/m^2, Isc=0.458 A, Pbat=4.77 W). Moderate represented transitional operation (480.10 W/m^2, Pbat=27.15 W) and contained the highest mean anomaly score (0.6563) and seven candidates. The High regime represented strong input (873.34 W/m^2, 50.00 °C, Pbat=45.89 W) but had PMPP,est=67.22 W, giving a mean residual of −21.33 W. This mismatch may reflect conversion, loading, estimation, temperature, and controller effects and is not interpreted as measured MPPT efficiency.

Despite its large mean residual, the High regime had the lowest mean anomaly score (0.3696), showing that the framework identifies multivariate rarity rather than simply large residual magnitude.

Table 4. Distribution of consensus regimes and anomaly candidates

Grouping	Low	Moderate	High	Anomaly candidates
Module P1	4	11	12	2
Module P3	8	8	11	5
Module P5	4	7	16	5
9 April 2026	2	13	3	7
20 April 2026	0	5	13	2
21 April 2026	9	2	4	0
23 April 2026	2	6	7	2
24 April 2026	3	0	12	1

P5 contained the largest High-regime share (16/27; 59.26%), while P3 was more evenly distributed and contained eight Low observations versus four each for P1 and P5. Regime composition varied strongly by day: High dominated 20 April (72.22%) and 24 April (80%), Low dominated 21 April (60%), and Moderate dominated 9 April (72.22%). This confirms that the five days sampled substantially different operating regimes.

3.3. Anomaly-Candidate Discovery and Interpretation

The anomaly-score distribution had Q_1=0.3333, a median of 0.5058, and Q_3=0.6768. The initial IQR upper fence was 1.1921, which exceeded the score range. Therefore, the program used the 95th percentile, producing a final main threshold of 0.831911.

Twelve observations, or 14.81% of the dataset, were selected by the mutually exclusive categorization. Five were high-score anomaly candidates with $A_i \geq 0.831911$. Seven additional observations were density-supported candidates because they were DBSCAN noise and had $Q_3 \leq A_i < 0.831911$. The remaining 69 observations were classified as non-anomalous. This three-group reporting separates strong composite-score evidence from density-supported evidence and prevents the two selection mechanisms from being conflated.

Table 5. Ranked high-score and density-supported candidates

Rank	Index	Module–day–time	State	Score	Residual (W)	Relative residual	Category
1	65	P3–23 Apr–13:30	Low	0.9153	3.5368	0.3165	High-score
2	7	P1–9 Apr–10:00	Moderate	0.8594	−10.0727	−0.2544	High-score
3	52	P1–23 Apr–09:30	Moderate	0.8572	24.6085	1.3924	High-score
4	81	P5–24 Apr–13:30	Low	0.8536	−8.6031	−0.5516	High-score
5	12	P5–9 Apr–11:30	Moderate	0.8319	−4.8523	−0.3596	High-score
6	9	P5–9 Apr–10:00	High	0.8236	−20.2805	−0.5652	Density-supported
7	2	P3–9 Apr–09:00	Moderate	0.8177	6.6013	0.1427	Density-supported
8	5	P3–9 Apr–09:30	Moderate	0.8064	−0.5436	−0.0128	Density-supported
9	8	P3–9 Apr–10:00	Moderate	0.7343	−2.2691	−0.0658	Density-supported
10	6	P5–9 Apr–09:30	High	0.7020	−6.7120	−0.1677	Density-supported
11	36	P5–20 Apr–14:30	Moderate	0.7020	7.0567	0.2994	Density-supported
12	35	P3–20 Apr–14:30	High	0.6989	−6.9616	−0.1893	Density-supported

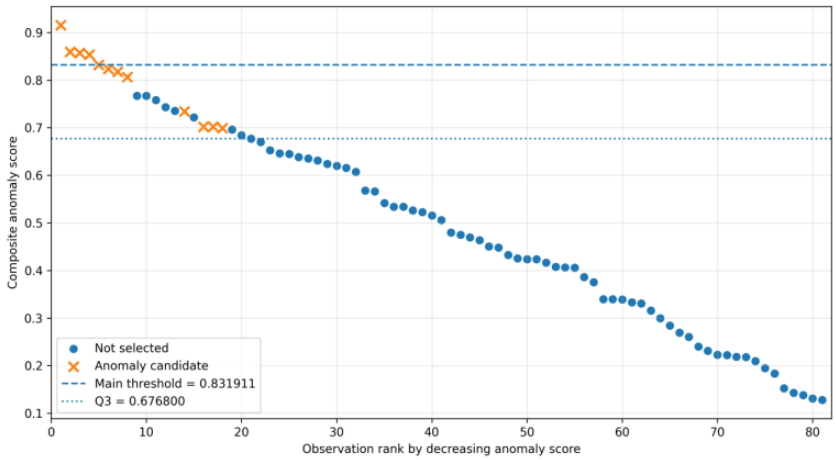


Figure 4. Ranked composite anomaly scores, including the high-score threshold and the third-quartile density-support boundary.

The highest-ranked high-score candidate was observation 65 (P3, 23 April 13:30; score 0.9153). Its residual was only 3.54 W, but GMM density, centroid/medoid distance, FCM uncertainty, and local sparsity were all high, demonstrating the benefit of multicomponent anomaly evidence.

Observation 52 (P1, 23 April) combined the largest positive candidate residual (24.61 W; relative residual 1.3924), DBSCAN-noise status, a score above the high-score threshold, and a physical diagnostic flag, giving the strongest convergence of residual, density, distance, and rule-based evidence. Observation 81 (P5, 24 April) was the only selected non-noise point; its high-score-threshold exceedance therefore confirms that the composite score is not equivalent to DBSCAN noise detection. Conversely, observation 5 (P3, 9 April) had a near-zero residual (−0.54 W) but remained density-supported because of local sparsity and cross-method disagreement, showing that structural anomaly evidence and residual magnitude are distinct.

Eleven of 14 DBSCAN noise points were selected, but three were not; only one of 67 non-noise points was selected. Likewise, only three of seven physical diagnostic observations overlapped with the 12 candidates, confirming complementary detection mechanisms. P3 and P5 each contained five candidates (18.52% of their 27 observations), while P1 contained two (7.41%). This does not establish a fault in P3; it only shows that P3 more often occupied sparse or disagreement-prone regions.

Seven candidates occurred on 9 April, two on 20 April, none on 21 April, two on 23 April, and one on 24 April. The concentration on 9 April indicates a day-specific pattern that warrants higher-resolution measurements or field inspection. The current dataset cannot determine whether these patterns arise from irradiance transients, controller response, measurement inconsistency, or module-specific behavior; no specific fault type is assigned.

3.4. Cross-Method Agreement, Reliability, and Limitations

The adjusted Rand index revealed major differences in how the algorithms partitioned the data. Pairwise ARI was used to distinguish agreement in partition structure from the internal validity of any single clustering solution. A high ARI indicates that two methods assign observations to similar groups despite their different modeling assumptions, whereas a low ARI indicates that they emphasize different geometric, fuzzy, probabilistic, or density structures. For comparisons involving DBSCAN, ARI was calculated on the 67 non-noise observations because 14 observations were labeled as noise. The resulting cross-method comparisons are summarized in Table 6.

Table 6. Selected pairwise partition agreements

Partition comparison	Observations used	ARI
K-Means vs FCM	81	0.0204
K-Means vs GMM	81	0.0797
K-Means vs K-Medoids	81	0.1445
FCM vs GMM	81	0.5949

Partition comparison	Observations used	ARI
FCM vs K-Medoids	81	0.3569
GMM vs K-Medoids	81	0.3232
K-Means vs DBSCAN	67	0.1221
FCM vs DBSCAN	67	0.5004
GMM vs DBSCAN	67	0.3371
K-Medoids vs DBSCAN	67	0.9301
Consensus vs FCM	81	0.5021
Consensus vs GMM	81	0.4514
Consensus vs K-Medoids	81	0.4913
Consensus vs DBSCAN	67	0.5469

The strongest agreement was K-Medoids–DBSCAN (ARI=0.9301 on 67 non-noise observations), providing independent support for a detailed five-state local structure. FCM–GMM agreement was moderate (ARI=0.5949), consistent with their non-crisp fuzzy and probabilistic representations. K-Means agreed poorly with the other methods (maximum base-method ARI=0.1445), consistent with its low repeated-run stability

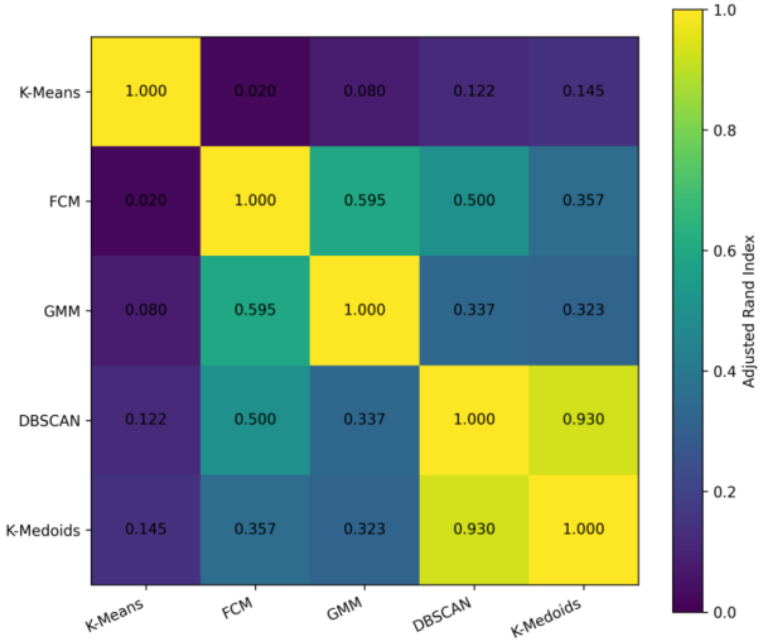


Figure 5. Adjusted Rand Index agreement among the five base clustering methods; DBSCAN comparisons use non-noise observations.

Consensus showed moderate agreement with FCM, GMM, K-Medoids, and DBSCAN (ARI=0.4514–0.5469), as expected when two-, three-, and five-state solutions are compressed into a common three-state ordinal representation. The study is limited by 81 observations over five days, the absence of verified fault labels, PMPP,est values not obtained from independent full I–V sweeps, and the lack of temporal-state modeling. Therefore, accuracy, sensitivity, specificity, and fault-class rates cannot be claimed. Nevertheless, physically ordered regime profiles, strong K-Medoids–DBSCAN agreement, and multi-criterion anomaly evidence support the framework as an exploratory screening tool for prioritizing field verification.

4. CONCLUSION

The operating data exhibited a reproducible but method-dependent cluster structure. Among the tested configurations, DBSCAN achieved the highest internal validity (Silhouette=0.3751; DBI=0.8749), while K-Medoids combined strong separation with high repeated-run stability (ARI=0.9655±0.0483); K-Means was substantially less stable (ARI=0.1261). The ordinal consensus yielded three physically interpretable operating regimes Low, Moderate, and High with 16, 26, and 39 observations, respectively, and mean battery-side power increasing from 4.77 to 27.15 and 45.89 W. Using the revised mutually exclusive

categorization, five observations were classified as high-score anomaly candidates ($A_i \geq 0.831911$), seven as density-supported candidates (DBSCAN noise with $Q_3 \leq A_i < 0.831911$), and the remaining 69 as non-anomalous. P3 and P5 each contained five selected candidates, and seven candidates occurred on 9 April 2026. Only three selected candidates also activated the physical diagnostic flag, indicating that rule-based and unsupervised screening capture complementary forms of unusual behavior. The strong K-Medoids–DBSCAN agreement (ARI=0.9301) supports the local structure, but the limited five-day dataset, absence of verified fault labels, and lack of independent I–V-curve measurements require all selected observations to be interpreted as candidates for physical verification rather than confirmed faults. Future work should extend the measurement period, include verified fault labels, and incorporate independent I–V characterization.

REFERENCES

[1] K. H. Hussein, I. Muta, T. Hoshino, and M. Osakada, "Maximum photovoltaic power tracking: An algorithm for rapidly changing atmospheric conditions," *IEE Proceedings Generation, Transmission and Distribution*, vol. 142, no. 1, pp. 59–64, 1995, doi: 10.1049/ip-gtd:19951577.

[2] A. Safari and S. Mekhilef, "Simulation and hardware implementation of Incremental Conductance MPPT with direct control method using Cuk converter," *IEEE Transactions on Industrial Electronics*, vol. 58, no. 4, pp. 1154–1161, 2011, doi: 10.1109/TIE.2010.2048834.

[3] W. Chine, A. Mellit, A. Massi Pavan, and S. A. Kalogirou, "Fault detection method for grid-connected photovoltaic plants," *Renewable Energy*, vol. 66, pp. 99–110, 2014, doi: 10.1016/j.renene.2013.11.073.

[4] F. Harrou, A. Dairi, B. Taghezouit, and Y. Sun, "An unsupervised monitoring procedure for detecting anomalies in photovoltaic systems using a one-class Support Vector Machine," *Solar Energy*, vol. 179, pp. 48–58, 2019, doi: 10.1016/j.solener.2018.12.045.

[5] Y. Cai, P. Lin, Y. Lin, Q. Zheng, S. Cheng, Z. Chen, and L. Wu, "Online photovoltaic fault detection method based on data stream clustering," I*OP Conference Series: Earth and Environmental Science*, vol. 431, no. 1, Art. no. 012060, 2020, doi: 10.1088/1755-1315/431/1/012060.

[6] G. M. Whyte, A. Gerber, U. Rau, and B. E. Pieters, "Anomaly detection, filtering and visualization for outdoor photovoltaic data," *Solar Energy*, vol. 307, Art. no. 114351, 2026, doi: 10.1016/j.solener.2026.114351.

[7] J. MacQueen, "Some methods for classification and analysis of multivariate observations," in *Proceedings of the Fifth Berkeley Symposium on Mathematical Statistics and Probability*, vol. 1, pp. 281–297, 1967.

[8] J. C. Bezdek, R. Ehrlich, and W. Full, "FCM: The fuzzy c-means clustering algorithm," *Computers & Geosciences*, vol. 10, nos. 2–3, pp. 191–203, 1984, doi: 10.1016/0098-3004(84)90020-7.

[9] A. P. Dempster, N. M. Laird, and D. B. Rubin, "Maximum likelihood from incomplete data via the EM algorithm," *Journal of the Royal Statistical Society*: Series B, vol. 39, no. 1, pp. 1–22, 1977, doi: 10.1111/j.2517-6161.1977.tb01600.x.

[10] M. Ester, H.-P. Kriegel, J. Sander, and X. Xu, "A density-based algorithm for discovering clusters in large spatial databases with noise," in *Proceedings of the Second International Conference on Knowledge Discovery and Data Mining*, pp. 226–231, 1996.

[11] L. Kaufman and P. J. Rousseeuw, *Finding Groups in Data: An Introduction to Cluster Analysis*. New York, NY, USA: Wiley, 1990, doi: 10.1002/9780470316801.

[12] P. J. Rousseeuw, "Silhouettes: A graphical aid to the interpretation and validation of cluster analysis," *Journal of Computational and Applied Mathematics*, vol. 20, pp. 53–65, 1987, doi: 10.1016/0377-0427(87)90125-7.

[13] D. L. Davies and D. W. Bouldin, "A cluster separation measure," *IEEE Transactions on Pattern Analysis and Machine Intelligence*, vol. PAMI-1, no. 2, pp. 224–227, 1979, doi: 10.1109/TPAMI.1979.4766909.

[14] T. Caliński and J. Harabasz, "A dendrite method for cluster analysis," *Communications in*

Statistics, vol. 3, no. 1, pp. 1–27, 1974, doi: 10.1080/03610927408827101.

[15] L. Hubert and P. Arabie, "Comparing partitions," *Journal of Classification*, vol. 2, no. 1, pp. 193–218, 1985, doi: 10.1007/BF01908075.

[16] G. D. Prenata and A. Ridho'i, "Evaluasi Komparatif K-Means dan Fuzzy C-Means sebagai Metode Klasterisasi Hard dan Soft untuk Analisis Perilaku Dielektrik Minyak Transformator Terkontaminasi Logam," JuTEkS (Jurnal Teknik Elektro dan Sains), vol. 13, no. 1, pp. 422–432, 2026.

[17] G. D. Prenata and A. Ridho'i, "Thermal Behavior Clustering of High-Voltage Electrical Equipment Using K-Means and Fuzzy C-Means," *Elkom: Jurnal Elektronika dan Komputer*, vol. 19, no. 1, pp. 229–238, 2026, doi: 10.51903/elkom.v19i1.3700.

[18] G. D. Prenata, M. A. S. Syariffudin, and R. S. Widagdo, "Application of Fourier Transform for Early Detection of Bearing Failures in Electric Motors," *Journal Geuthee of Engineering and Energy (JOGE)*, vol. 5, no. 1, pp. 24–32, 2026, doi: 10.52626/joge.v5i1.69.

[19] G. D. Prenata, A. Ridho'i, and M. R. Arshad, "Comparative Evaluation of LSTM and Metaheuristic-Optimized Neural Networks for ECG Prediction under Limited Data Conditions," *Journal of Electronics, Electromedical Engineering, and Medical Informatics*, vol. 8, no. 2, pp. 751–768, 2026, doi: 10.35882/jeeemi.v8i2.1524.

[20] F. H. Limbong, T. Taufiq, and A. Bintoro, "System Monitoring of Solar Power Plant Using NODE MCU ESP8266 Based on IoT," *Journal Geuthee of Engineering and Energy (JOGE)*, vol. 3, no. 2, pp. 84–95, 2024, doi: 10.52626/joge.v3i2.43.

[21] C. W. Azzahra, Muhammad, and I. Mahmudi, "Evaluation Study of Solar Powered Public Street Lighting as Battery Charging at Islamic Center Based on PSIM," *Journal Geuthee of Engineering and Energy (JOGE)*, vol. 3, no. 2, pp. 51–58, 2024, doi: 10.52626/joge.v3i2.41.